

Coupling of magnon modes in nanodisk with spin texture

Zijie Zhou(周子杰), Junning Zhao(赵俊宁), Xinhui Ma(马心慧), Rong Wang(王熔), and Fusheng Ma(马付胜)
Citation: Chin. Phys. B, 2025, 34 (**10**): 107506. DOI: 10.1088/1674-1056/ade426
http://cpb.iphy.ac.cn; http://iopscience.iop.org/cpb

What follows is a list of articles you may be interested in

Bifurcation of the bound states in the continuum in a dissipative cavity magnonic system

Xinlin Mi(米锌林), Lijun Yan(闫丽君), Bimu Yao(姚碧霖), Shishen Yan(颜世申), Jinwei Rao(饶金威), and Lihui Bai(柏利慧)
Chin. Phys. B, 2025, 34 (**6**): 067508. DOI: 10.1088/1674-1056/add4e4

Multiferroicity and thermal expansion of the layered metal-organic framework $[NH_4Cl]_2[Ni(HCOO)_2(NH_3)_2]$

Dan Cheng(程丹), Yingjie He(何英杰), Shuang Liu(刘爽), Na Su(苏娜), and Young Sun(孙阳)
Chin. Phys. B, 2025, 34 (**6**): 067505. DOI: 10.1088/1674-1056/adcaa4

Perpendicular magnetic anisotropy of Pd/Co_2MnSi/Co/Pd multilayer

Xiaoqi Qin(秦晓奇), Jiaxing Tan(谭家兴), Xianwu Xiu(修显武), Wentian Cao(曹文田), and Shuyun Wang(王书运)
Chin. Phys. B, 2025, 34 (**3**): 037502. DOI: 10.1088/1674-1056/ada694

Alternating spin splitting of electronic and magnon bands in two-dimensional altermagnetic materials

Qian Wang(王乾), Da-Wei Wu(邬大为), Guang-Hua Guo(郭光华), Meng-Qiu Long(龙孟秋), and Yun-Peng Wang(王云鹏)
Chin. Phys. B, 2024, 33 (**9**): 097507. DOI: 10.1088/1674-1056/ad6425

First-principles study of electronic and magnetic properties of Fe atoms on Cu_2N/Cu(100)

Jiale Chen(陈佳乐) and Jun Hu(胡军)
Chin. Phys. B, 2024, 33 (**8**): 087502. DOI: 10.1088/1674-1056/ad5275

SPECIAL TOPIC — Advanced magnonics

Coupling of magnon modes in nanodisk with spin texture

Zijie Zhou(周子杰), Junning Zhao(赵俊宁), Xinhui Ma(马心慧), Rong Wang(王熔), and Fusheng Ma(马付胜)†

Key Laboratory of State Manipulation and Advanced Materials in Provincial Universities, Institute of Physics Frontiers and Interdisciplinary Sciences, School of Physics and Technology, Nanjing Normal University, Nanjing 210046, *China*

(Received 31 March 2025; revised manuscript received 12 June 2025; accepted manuscript online 13 June 2025)

Magnetic nanostructures with nonhomogeneous magnetic properties exhibit distinct magnon modes, and their interactions are crucial for understanding magnetization dynamics. In this work, we numerically investigate the magnon–magnon coupling in a nanodisk with radially varying magnetic anisotropy by using micromagnetic simulations. By introducing perpendicular magnetic anisotropy into the inner region of the nanodisk, a radially chiral spin texture is observed. The presence of the chiral spin texture results in coupling between the ferromagnetic resonance mode of the whole disk and the higher-order confined modes in the outer region. Moreover, we find that the coupling strength is highly sensitive to the perpendicular magnetic anisotropy, the saturation magnetization, and the interfacial Dzyaloshinskii–Moriya interaction. Our findings could enrich the understanding of the dynamic characteristics of chiral nanomagnets and suggest a possible route to harnessing tunable magnon–magnon coupling for spin-based quantum information processing.

Keywords: coupling, magnon, chiral spin texture, micromagnetic simulation

PACS: 75.30.Gw, 75.78.Cd, 75.75.–c, 75.78.–n

DOI: 10.1088/1674-1056/ade426 **CSTR:** 32038.14.CPB.ade426

1. Introduction

Magnetic chirality refers to the handedness of spin arrangements, a characteristic commonly found in certain spin-ordered states or nanoscale spin textures.[1–5] The Dzyaloshinskii–Moriya interaction (DMI) is recognized as a fundamental interaction that induces the formation of chiral spin structures such as magnetic skyrmions.[6,7] In magnetic thin films, the interfacial DMI is the principal mechanism that gives rise to distinctive chiral spin textures, i.e., chiral domain walls,[8] spin spirals,[9] radial vortices,[10–12] and skyrmions.[13,14] Chiral spin textures hold great promise for realizing information storage and processing functions, such as racetrack memory,[15] logic devices,[16] transistors, oscillators,[13] and frequency combs,[16] thereby significantly facilitating the development of novel spintronic devices.

Cavity magnonics has attracted great attention due to its potential applications in coherent information processing.[17–20] As quanta of spin waves, magnons possess short wavelengths, high frequencies (up to the terahertz regime), non-Ohmic dissipation, and easy tunability.[21–23] These advantages open the possibility of developing energy-efficient magnonic devices for quantum information operations.[24,25] The coupling between magnons and other quasiparticles or excitations has been studied in a variety of systems, such as magnon–photon,[26–28] magnon–magnon,[29,30] magnon–phonon,[31–33] and magnon–superconducting-qubit interactions.[34–36] Among them, magnon–magnon coupling has been investigated toward the miniaturization and integration of spintronic devices.[37–40] The coupling between the ferromagnetic resonance (FMR) mode and the standing spin-wave (SSW) mode has been reported in Ni/YIG and Co/YIG heterostructures, respectively.[28,30] Recent studies have demonstrated that the coupling between the optical mode and the acoustic mode in synthetic antiferromagnets can reach the strong, ultra-strong, and deep-strong regimes.[41–43] The magnon–magnon coupling within an individual magnetic single layer has also been realized in, for instance, an irregular hexagonal dot and a cross-shaped nanoring.[44–48] Very recently, it has been found that magnetic nanostructures with nonhomogeneous material properties can exhibit diverse spin configurations in the presence of interfacial DMI.[2] The coupling between magnon modes confined in such nonhomogeneous magnetic nanostructures is therefore worth exploring.

In this work, we perform micromagnetic simulations to numerically investigate the coupling between magnons in a magnetic nanodisk with radially varying magnetic anisotropy. The chiral spin texture is obtained by introducing the interfacial DMI and the radially distributed perpendicular magnetic anisotropy (PMA). We find that the FMR mode of the entire nanodisk can couple with various radial modes confined in the outer ring-shaped (OR) region. The tunability of the coupling is verified by varying the PMA, saturation magnetization, and interfacial DMI. Our findings demonstrate that chiral nanomagnets could serve as an excellent platform for exploring coupling phenomena within the field of cavity magnonics.

†Corresponding author. E-mail: phymafs@njnu.edu.cn

© 2025 Chinese Physical Society and IOP Publishing Ltd. All rights, including for text and data mining, AI training, and similar technologies, are reserved.

2. Model and simulation method

Figure 1(a) schematically shows the magnetic nanodisk used, with a spatially distributed magnetic anisotropy along the radial direction, i.e., the inner circular (IC) region possesses PMA. The diameters of the nanodisk and the IC region are represented by d_1 and d_2, respectively. The micromagnetic simulations are performed using Mumax^3.[49] During the simulations, the nanodisk is discretized into cubic cells with a size of 1 nm × 1 nm × 1 nm along the x, y, and z axes, respectively. The material parameters used in the simulations are adopted from the Pt/Co/Al system: saturation magnetization $M_s = 9\times10^5$ A/m, exchange stiffness constant $A = 1.6\times10^{-11}$ J/m, interfacial DMI constant $D = 1.5\times10^{-3}$ J/m^2, damping constant $\alpha = 0.01$, and PMA constant $K_u = 5.7\times10^5$ J/m^3.[2,47]

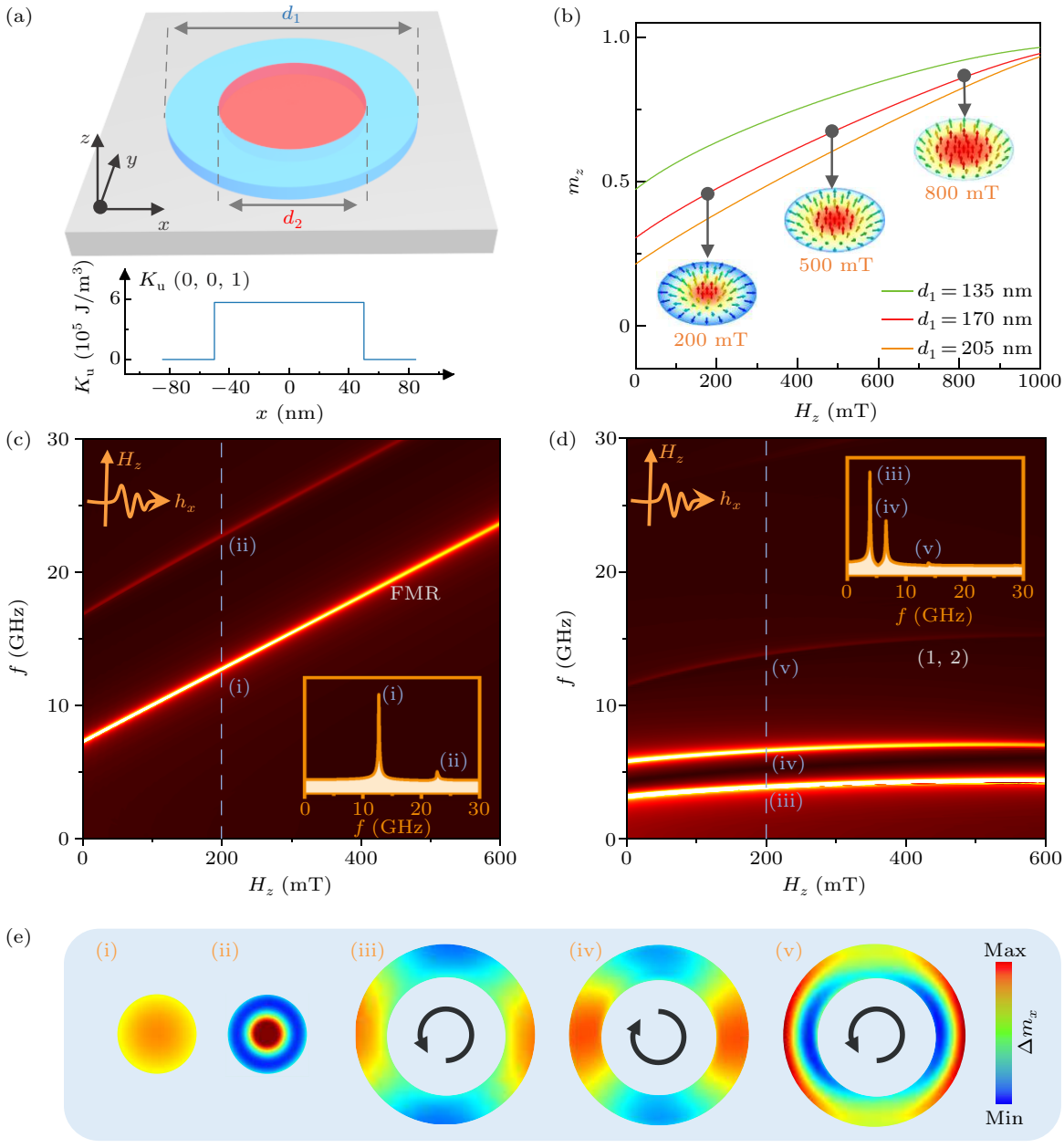


Fig. 1. (a) Schematic illustration of the magnetic nanodisk with radially varying magnetic anisotropy. The red and blue regions represent the IC and OR regions, respectively. (b) The fraction of m_z–H_z curves for a fixed $d_2 = 100$ nm and various $d_1 = 135$ nm, 170 nm, and 205 nm. Insets show the magnetization distributions for $d_1 = 170$ nm under three typical fields. Color plots of the f–H_z dispersion for (c) the IC region and (d) the OR region. Insets display the corresponding magnon spectra at $H_z = 200$ mT. (e) Normalized mode profiles of the magnon modes labeled as (i)–(v) in (c) and (d).

The magnetization distribution and magnon modes under different bias fields H_z are calculated through a two-step simulation procedure. Firstly, the magnetization distribution is obtained by minimizing the total energy of the system under each H_z. Secondly, to excite magnons with frequencies ranging from 0 GHz to 100 GHz, a spatially uniform sinc-function-type perturbation field of the form $h_{rf}(t) = h_0 \sin(2\pi f_c t)/(2\pi f_c t)$ is applied along the x-axis, where the

amplitude is $h_0 = 5$ mT and the cut-off frequency is $f_c = 100$ GHz.[50] Alternatively, to excite magnons at a fixed frequency f and to obtain the corresponding mode profiles, a sinusoidal perturbation field $h_x(t) = h_0 \sin(2\pi f t)$ is applied along the x-axis. For the dynamic simulations under each H_z, the temporal evolution of the spatially averaged magnetization $m(t)$ is recorded, with a time step of $\Delta t = 10$ ps. The magnon spectra are obtained by performing a fast Fourier transform (FFT) on the spatially averaged $m_x(t)$. The mode profiles of magnons are characterized by temporal snapshots of the magnetization variation, defined as $\Delta m_x(t) = m_x(t) - m_x(0)$.

3. Results and discussion

The investigated nanodisk consists of two regions: the IC region with perpendicular magnetic anisotropy $K_u = 5.7 \times 10^5$ J/m^3 along the z-axis, and the OR region with zero K_u, as schematically illustrated in Fig. 1(a). The calculated magnetization–field (m_z–H_z) loops of the nanodisk are shown in Fig. 1(b) for $d_2 = 100$ nm and $d_1 = 135$ nm, 170 nm, and 205 nm. The slope of the magnetization curve increases with larger d_1. The insets in Fig. 1(b) display the magnetization distributions for $d_1 = 170$ nm at $H_z = 200$ mT, 500 mT, and 800 mT, respectively. The observed chiral spin textures arise from the competition among DMI, exchange interaction, and magnetic anisotropy.

We first focus on the nanodisk with $d_1 = 170$ nm, as shown in Figs. 1(c) and 1(d). The magnon spectra of the IC and OR regions are separately calculated, and the corresponding frequency–field (f–H_z) dispersions are presented in Figs. 1(c) and 1(d). Figure 1(d) shows the f–H_z dispersion of the OR region alone, with the magnetization of the IC region fixed. The fixed out-of-plane magnetization in the IC region still exerts a significant static influence on the magnon modes confined within the OR region. This interaction disturbs the spatial uniformity required for coherent precession, thereby suppressing the visibility of the FMR mode in the OR region.

For the IC region, two distinct magnon modes, labeled (i) and (ii), are identified in Fig. 1(c). The inset shows the corresponding spectrum at $H_z = 200$ mT. Based on the spatial mode profiles in Fig. 1(e), mode (i) is recognized as the first radial mode (the ferromagnetic resonance, or FMR mode), characterized by a nearly uniform precession without radial nodes. Mode (ii) is identified as the second radial mode, exhibiting a single radial node in the magnetization distribution.

In contrast, for the unsaturated OR region, three distinct magnon modes, (iii), (iv), and (v), are observed, as indicated in Fig. 1(c). These modes exhibit combined azimuthal and radial characteristics and can be indexed by (radial, azimuthal) numbers. They correspond to the spatially confined (0, +2), (0, −2), and (1, +2) modes, respectively, as shown in Fig. 1(e). For clarity, the color maps of all mode profiles in Fig. 1(e) are individually normalized to their maximum Δm_x amplitude. Modes (iii) and (iv) are low-frequency gyrotropic modes, with the signs +/− denoting counterclockwise/clockwise propagation directions. Mode (v), having a higher frequency than (iii) and (iv), exhibits counterclockwise propagation and features one azimuthal and two radial nodes. Although some modes share the same azimuthal number m, differences in their radial node numbers lead to distinct spatial distributions.

Next, Fig. 2(a) presents the f–H_z color plot of the nanodisk with $d_1 = 170$ nm and $d_2 = 100$ nm. The high- and low-frequency branches clearly exhibit coupling features, such as the characteristic "anti-crossing" behavior and pronounced intensity exchange. The coupling parameters are analyzed as follows: the coupling strength $g = |f_1 - f_2|/2$, the coupling magnetic field H_g, and the coupling center frequency $f_g = |f_1 + f_2|/2$, where f_1 and f_2 are the frequencies of the upper and lower magnon modes at H_g.

To identify which magnon modes participate in the coupling, we extract the mode frequencies in the IC region, OR region, and the whole nanodisk, as shown in Fig. 2(b). Figure 2(c) shows the radial intensity distributions of the FMR mode, the (1, +2) mode, and the coupling mode (CM) for $H_z =$ 320 mT. The temporal variation of magnetization $\Delta m_x(x,t)$ along the radius is normalized to indicate the relative magnon intensity.[50] The intensity distributions reflect the overall dynamic response of the coupled state. It can be seen that the (1, +2) mode strongly influences the precession near the IC–OR interface, while the FMR mode extends across the entire nanodisk. The CM exhibits a hybridized character that combines features of both.

To further verify the mode origins, Fig. 2(d) displays normalized Δm_x intensity maps of modes I–IV (labeled in Fig. 2(b)). Each color map is normalized to its own maximum value. At $H_z = 320$ mT (near H_g), the profiles of modes I and II indicate strong hybridization between the FMR and (1, +2) modes. At $H_z = 600$ mT (far from H_g), the hybridization largely vanishes, as shown by modes III and IV. Furthermore, Fig. 2(e) presents the radial intensity distributions of modes I–IV at $t = 0$ and $T/2$, marked by the dashed lines in Fig. 2(d). The results show that mode III corresponds to the (1, +2) mode, mode IV to the FMR mode, and mode II to the coupled mode, which is a superposition of both.

Compared with the FMR mode, the (1, +2) mode exhibits a weaker magnetic-field dependence, allowing the two magnon modes to intersect and couple. Higher-order radial magnon modes have a similar f–H_z slope to that of the first radial mode, implying that coupling with the FMR mode is also possible.

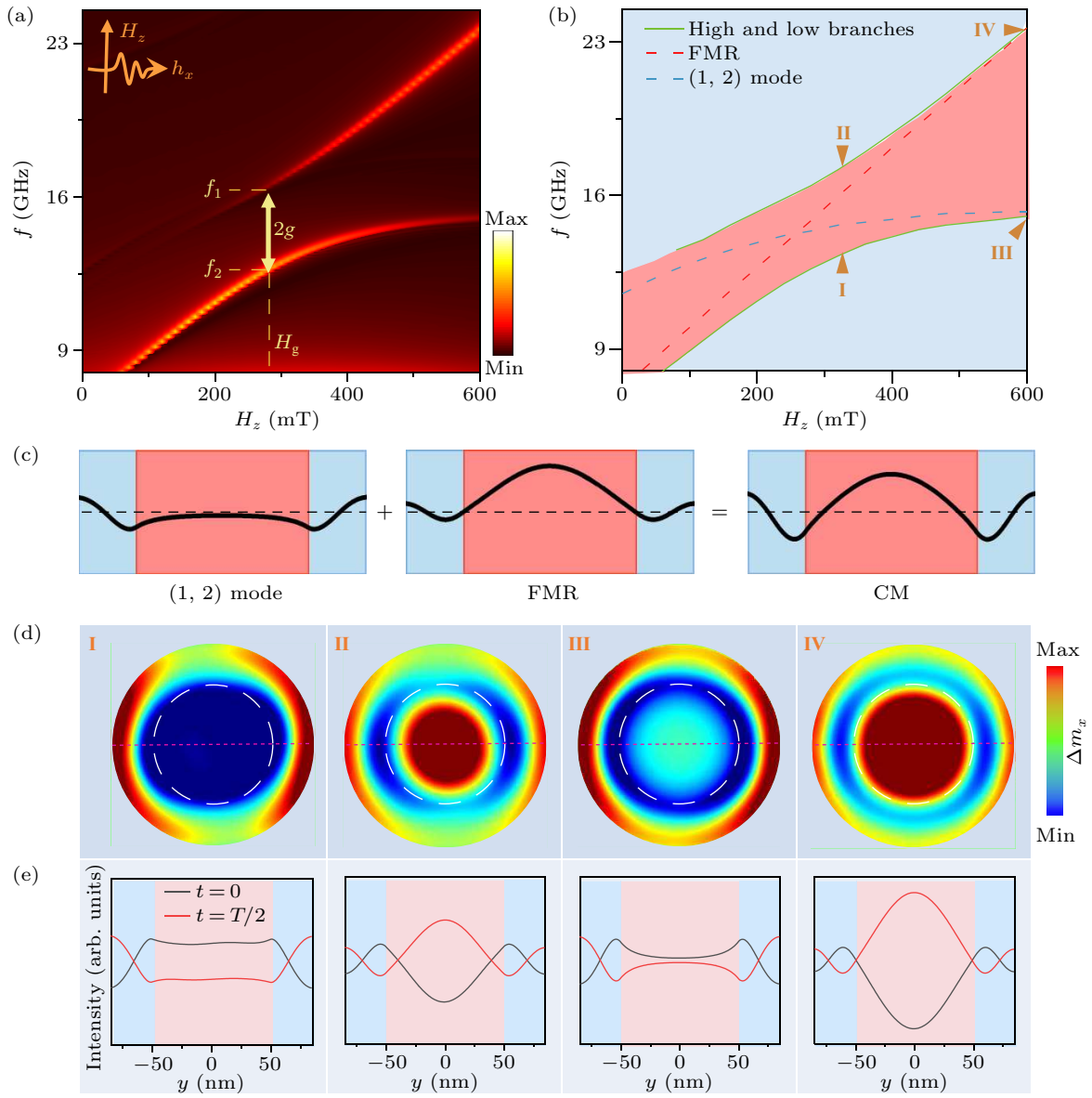


Fig. 2. (a) Color plots of the f–H_z dispersion for a magnetic nanodisk with $d_1 = 170$ nm and $d_2 = 100$ nm. (b) Extracted f–H_z dispersion of the high- and low-frequency branches (green lines) from (a), the FMR mode (i) (red dashed line) extracted from Fig. 1(c), and the confined mode (v) (blue dashed line) extracted from Fig. 1(d). (c) Conceptual illustration of the magnon intensity in the nanodisk along the radius: the (1, +2) mode, FMR mode, and CM. (d) Mode profiles of magnon modes I–IV as marked in panel (b). Dashed circles represent the boundaries between the IC and OR regions. (e) Intensity distributions of magnon modes I–IV along the radial direction, labeled by horizontal dotted lines in panel (d) for $t = 0$ and $T/2$. The red and blue backgrounds represent the IC and OR regions, respectively.

According to the characteristics of radial magnons, higher-order radial modes can be excited by increasing the diameter of the OR region. As an example, Fig. 3(a) shows the color plots of the f–H_z dispersion obtained for $d_1 = 190$ nm and $d_2 = 100$ nm. The intensity distributions of Δm_x along the radius for various magnon modes b, c, d, and e are shown in Figs. 3(b)–3(e), respectively, as labeled by triangles in Fig. 3(a). It is clearly observed that modes c and e are FMR modes, while modes b and d are confined modes in the OR region with different node configurations, (1, +2) and (2, +2). In Fig. 3(a), the lower anti-crossing arises from the coupling between the FMR mode and the (1, +2) mode, whereas the higher anti-crossing results from the coupling between the FMR mode and the (2, +2) mode. Therefore, it is expected that the coupling between the FMR mode and even higher-order radial magnon modes can be achieved by further increasing d_1.

To investigate the influence of magnetic parameters on the coupling, we study the nanodisk by varying D, K_u, and M_s, respectively.

First, Fig. 4(c) illustrates the effect of M_s in the range from 8.1×10^5 A/m to 9.9×10^5 A/m. It is observed that g and f_g decrease from 2.39 GHz to 1.63 GHz and from 14.84 GHz to 13.68 GHz, while H_g increases from 41 mT to 470 mT. The increasing M_s enhances the demagnetizing field, which flattens the magnetization at the boundary between the IC and OR regions, i.e., broadens the transition region.[51] This reduced spatial overlap between the magnon modes suppresses

the coupling strength.[52]

Second, the effect of K_u in the IC region is examined within the range from 5.1×10^5 J/m^3 to 6.3×10^5 J/m^3, as shown in Fig. 4(b). H_g, g, and f_g exhibit distinct dependences on K_u: g increases from 1.79 GHz to 2.06 GHz, H_g decreases from 410 mT to 150 mT, and f_g remains nearly constant around 14.50 GHz. The increasing K_u enhances the out-of-plane alignment of magnetization in the IC region, causing the transition region at the IC–OR boundary to become narrower.[53] This leads to increased spatial overlap between the magnon modes, thereby enhancing the coupling strength. Moreover, a higher K_u strengthens the internal effective field and raises the intrinsic resonance frequency of the IC region, shifting the mode crossing point to a lower external field.

Third, the dependence of H_g, g, and f_g on D is shown in Fig. 4(a). With D increasing from 1.5 to 2.5×10^{-3} J/m^2, g decreases from 1.90 GHz to 1.66 GHz, f_g increases from 14.55 GHz to 16.38 GHz, and H_g increases from 280 mT to 340 mT. With increasing D, the DMI favors non-collinear alignment between the magnetizations in the IC and OR regions, thereby enlarging the angular deviation and broadening the magnetization transition region. This reduces the spatial overlap between the FMR and (1, +2) modes, thus weakening the coupling strength.[54] A stronger external field H is required to overcome this non-collinear tendency, leading to an increase in H_g. Since the coupling occurs within a single-layer nanodisk, it is primarily mediated by exchange interaction, which dominates when the interacting spin-wave modes exhibit strong spatial overlap, while the dipolar interaction plays a negligible role in such confined geometries.[55–57]

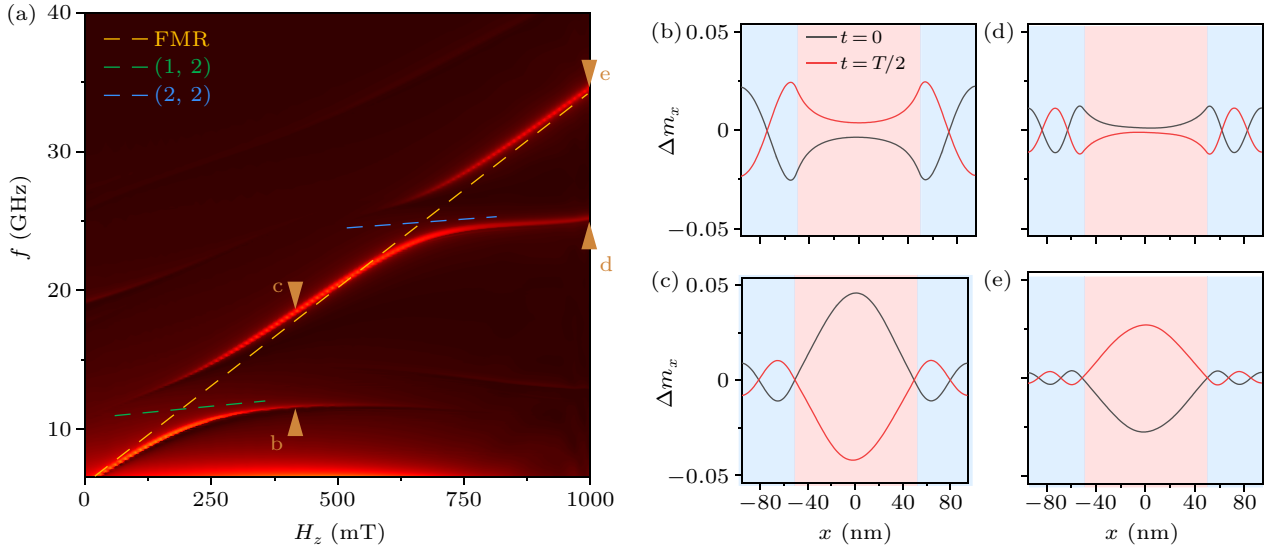


Fig. 3. (a) Color plots of the f–H_z dispersion for a magnetic nanodisk with $d_1 = 190$ nm and $d_2 = 100$ nm. The lower anti-crossing represents the coupling between the FMR mode (orange dashed line) and the (1, +2) mode (green dashed line), while the higher anti-crossing represents the coupling between the FMR mode and the (2, +2) mode (blue dashed line). (b)–(e) Intensity distributions of magnon modes b, c, d, and e along the radial direction, as labeled by triangles in (a), for $t = 0$ and $T/2$. The red and blue backgrounds represent the IC and OR regions, respectively.

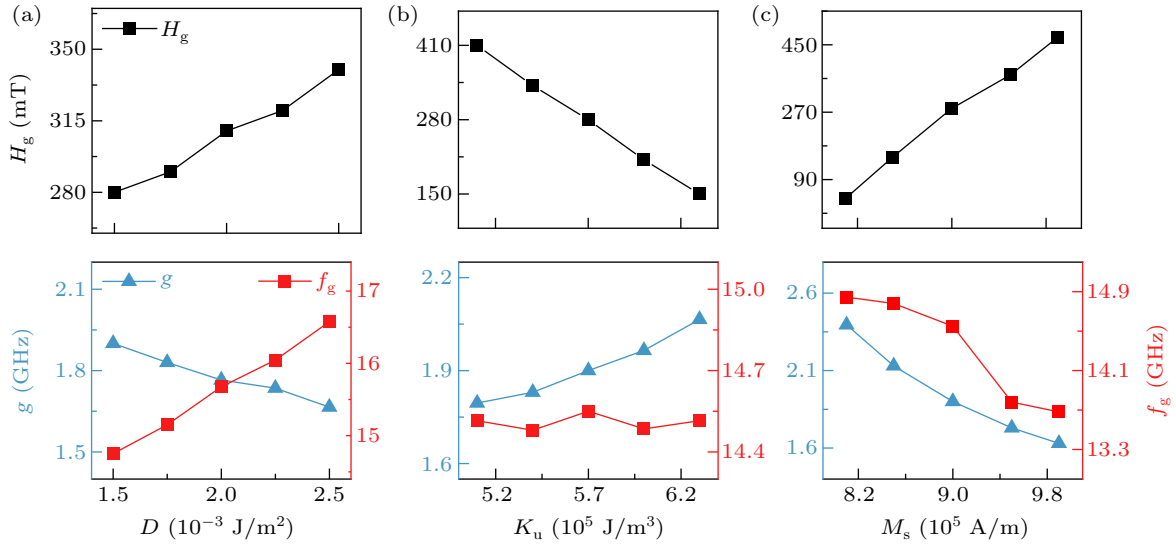


Fig. 4. The H_g, g, and f_g as functions of D, K_u, and M_s: (a) $K_u = 5.7 \times 10^5$ J/m^3 and $M_s = 9 \times 10^5$ A/m; (b) $M_s = 9 \times 10^5$ A/m, and $D = 1.5 \times 10^{-3}$ J/m^2; (c) $D = 1.5 \times 10^{-3}$ J/m^2 and $K_u = 5.7 \times 10^5$ J/m^3.

4. Conclusion

In summary, we numerically study the magnon–magnon coupling in a magnetic nanodisk with a radially chiral spin texture, which is realized through the introduction of interfacial DMI and radially distributed PMA. The observed coupling is attributed to the interaction between the FMR mode of the entire nanodisk and the higher-order confined modes in its outer ring-shaped region. It is also found that the coupling phenomena are highly sensitive to D, K_u, and M_s. The coupling strength increases with K_u but decreases with D and M_s. This work provides new insights into the dynamic characteristics of chiral nanomagnets, highlighting them as a promising platform for exploring magnon coupling phenomena.

Acknowledgments

This work was supported by the National Key Research and Development Program of China (Grant No. 2023YFF0718400) and the National Natural Science Foundation of China (Grant Nos. 12474119 and 12074189).

References

[1] Eslami S, Gibbs J G, Rechkemmer Y, Slageren J V, Alarcon-Correa M, Lee T C, Mark A G, Rikken G L J A and Fischer P 2014 *ACS Photonics.* **1** 11
[2] Luo Z C, Dao T P, Hrabec A, Vijayakumar J, Kleibert A, Baumgartner M, Kirk E, Cui J, Savchenko T, Krishnaswamy G, Heyderman L J and Gambardella P 2019 *Science* **363** 1435
[3] Yang S H, Naaman R, Paltiel Y and Parkin S S P 2021 *Nat. Rev. Phys.* **3** 328
[4] Cheong S and Xu X H 2022 *Npj Quantum Mater.* **7** 40
[5] Yu T, Luo Z C and Bauer G E W 2023 *Phys. Rep.* **1009** 1
[6] Dvořák V 1971 *Phys. Status Solidi.* **46** 763
[7] Moriya T 1960 *Phys. Rev.* **120** 91
[8] Vélez S, Schaab J, Wörnle M S, Müller M, Gradauskaite E, Welter P, Gutgsell C, Nistor C, Degen C L, Trassin M, Fiebig M and Gambardella P 2019 *Nat. Commun.* **10** 4750
[9] Bode M, Heide M, Bergmann K V, Ferriani P, Heinze S, Bihlmayer G, Kubetzka A, Pietzsch O, Blügel S and Wiesendanger R 2007 *Nature* **447** 190
[10] Siracusano G, Tomasello R, Giordano A, Puliafito V, Azzerboni B, Ozatay O, Carpentieri M and Finocchio G 2016 *Phys. Rev. Lett.* **117** 087204
[11] Li H N, Xue T X, Chen L, Sui Y R and Wei M B 2022 *Chin. Phys. B* **31** 097501
[12] Yang M S, Fang L and Chi Y Q 2018 *Chin. Phys. B* **27** 098504
[13] Fert A, Reyren N and Cros V 2017 *Nat. Rev. Mater.* **2** 17031
[14] Heinze S, Bergmann K V, Menzel M, Brede J, Kubetzka A, Wiesendanger R, Bihlmayer G and Blügel S 2011 *Nat. Phys.* **7** 713
[15] Parkin S S P, Hayashi M and Thomas L 2008 *Science* **320** 190
[16] Wang Z Y, Yuan H Y, Cao Y S, Li Z X, Duine R A and Yan P 2021 *Phys. Rev. Lett.* **127** 037202
[17] Lachance-Quirion D, Tabuchi Y, Gloppe A, Usami K and Nakamura Y 2019 *Appl. Phys. Express* **12** 070101
[18] Li Y, Zhang W, Tyberkevych V, Kwok W K, Hoffmann A and Novosad V 2020 *J. Appl. Phys.* **128** 130902
[19] Pirro P, Vasyuchka V, Serga A and Hillebrands B 2021 *Nat. Rev. Mater.* **6** 1114
[20] Lan G B, Liu K Y, Wang Z Y, Xia F, Xu H J, Guo T Y, Zhang Y, He B, Li J H, Wan C H, Bauer G E W, Yan P, Liu G Q, Pan X Y, Han X F and Yu G Q 2025 *Nat. Commun.* **16** 1178
[21] Liu H F, Ali S S and Han X F 2014 *Chin. Phys. B* **23** 077501
[22] Chumak A V, Vasyuchka V I, Serga A and Hillebrands B 2015 *Nat. Phys.* **11** 453
[23] Han X F, Tao L L, Wu H, Tang P and Xing Y W 2023 *J. Phys. D: Appl. Phys.* **56** 443001
[24] Choudhury S, Chaurasiya A K, Mondal A K, Rana B, Miura K, Takahashi H, Otani Y C and Barman A 2020 *Sci. Adv.* **6** 5457
[25] Yuan H Y, Cao Y S, Kamra A, Duine R and Yan P 2022 *Phys. Rep.* **965** 1
[26] Zhang X, Zou C L, Jiang L and Tang H X 2014 *Phys. Rev. Lett.* **113** 156401
[27] Hou J T and Liu L 2019 *Phys. Rev. Lett.* **123** 107702
[28] Li Y, Polakovic T, Wang Y L, Xu J, Lendinez S, Zhang Z, Ding J, Khaire T, Saglam H, Divan R, Pearson J, Kwok W K, Xiao Z, Novosad V, Hoffmann A and Zhang W 2019 *Phys. Rev. Lett.* **123** 107701
[29] Klingler S, Amin V, Geprägs S, Ganzhorn K, Maier-Flaig H, Althammer M, Huebl H, Gross R, McMichael R D, Stiles M D, Goennenwein S T B and Weiler M 2018 *Phys. Rev. Lett.* **120** 127201
[30] Chen J L, Liu C P, Liu T, Xiao Y, Xia K, Bauer G E W, Wu M and Yu H M 2018 *Phys. Rev. Lett.* **120** 217202
[31] Berk C, Jaris M, Yang W G, Dhuey S, Cabrini S and Schmidt H 2019 *Nat. Commun.* **10** 2652
[32] Zhang X F, Zou C L, Jiang L and Tang H X 2016 *Sci. Adv.* **2** e1501286
[33] Li J, Zhu S Y and Agarwal G S 2018 *Phys. Rev. Lett.* **121** 203601
[34] Morris R G E, Loo A F V, Kosen S and Karenowska A D 2017 *Sci. Rep.* **7** 11511
[35] Tabuchi Y, Ishino S, Noguchi A, Ishikawa T, Yamazaki R, Usami K and Nakamura Y 2015 *Science* **349** 405
[36] Tabuchi Y, Ishino S, Noguchi A, Ishikawa T, Yamazaki R, Usami K and Nakamura Y 2016 *C. R. Phys.* **17** 729
[37] Tang J, Ke Y J, He W, Zhang X Q, Zhang W, Li N, Zhang Y S, Li Y and Cheng Z H 2018 *Adv. Mater.* **30** 1706439
[38] Shiota Y, Taniguchi T, Ishibashi M, Moriyama T and Ono T 2020 *Phys. Rev. Lett.* **125** 017203
[39] Chen L N, Gao Z Y, Zhou K Y, Du Y W and Liu R H 2021 *Phys. Rev. Appl.* **16** 034004
[40] Sheng L T, Mehrdad E, Chen J L, He W Q, Wang Y Z, Wang H C, Feng H M, Zhang Y, Israa M, Liu S, Jiang W J, Han X F, Yu D P, Jean-Philippe A, Gerrit E W B and Yu H M 2023 *Phys. Rev. Lett.* **130** 046701
[41] Dai C T and Ma F S 2021 *Appl. Phys. Lett.* **118** 112405
[42] Xiao X, Chen Z D, Dai C T and Ma F S 2022 *J. Appl. Phys.* **131** 093905
[43] Wang Y Q, Zhang Y, Li C Z, Wei J W, He B, Xu H J, Xia J H, Luo X M, Li J H, Dong J, He W Q, Yan Z R, Yang W L, Ma F S, Chai G Z, Yan P, Wan C H, Han X F and Yu G Q 2024 *Nat. Commun.* **15** 2077
[44] Berk C, Jaris M, Yang W G, Dhuey S, Cabrini S and Schmidt H 2019 *Nature Commun.* **10** 2652
[45] Tsymbal 2020 *Appl. Phys. Lett.* **77** 2740
[46] Krishnia S, Haltz E, Berges L, Aballe L, Foerster M, Bocher L, Weil R, Thiaville A and Sampaio J 2021 *Phys. Rev. Appl.* **16** 024040
[47] Dai C T, Xie K L, Pan Z Z and Ma F S 2020 *J. Appl. Phys.* **127** 203902
[48] Adhikari K, Choudhury S, Barman S, Otani Y and Barman A 2021 *Nat. Nanotechnol.* **32** 395706
[49] Vansteenkiste A, Leliaert J, Dvornik M, Helsen M, Garcia-Sanchez F and Waeyenberge B V 2014 *AIP Adv.* **4** 107133
[50] Ma F S, Zhou Y, Braun H B and Lew W S 2015 *Nano Lett.* **15** 4029
[51] Zhang T F, Wang Q W, Chen M, Dong J, Zhao Q, Li Z M, Liu Q F, Wang J B and Wei J W 2025 *Chin. Phys. B* **34** 057201
[52] Chen J L, Liu C P, Liu T, Xiao Y, Xia K, Bauner G E W, Wu M Z and Yu H M 2018 *Phys. Rev. Lett.* **120** 217202
[53] DeJong M D, and Livesey K L 2015 *Phys. Rev. B* **92** 214420
[54] Siracusano G, Tomasello R, Giordano A, Puliafito V, Azzerboni B, Ozatay O, Carpentieri M and Finocchio G 2016 *Phys. Rev. Lett.* **117** 087204
[55] Moaloc M, Zelent M, Szulc K and Krawczyk M 2024 *Sci. Rep.* **14** 11501
[56] Dion T, Stenning K D, Vanstone A, Holder H H, Sultana R, Alatteili G, Martinez V, Kaffash M T, Kimura T, Oulton R F, Branford W R, Kurebayashi H, Iacocca E, Jungfleisch M B and Gartside J C 2024 *Nat. Commun.* **15** 4077
[57] Santos F J, Dias M and Lounis S 2020 *Phys. Rev. B* **102** 104401